Science Advances
AAAS

advances.sciencemag.org/cgi/content/full/7/14/eabd3632/DC1

Supplementary Materials for

Earth's carbon deficit caused by early loss through irreversible sublimation

J. Li*, E. A. Bergin, G. A. Blake, F. J. Ciesla, M. M. Hirschmann

*Corresponding author. Email: jackieli@umich.edu

Published 2 April 2021, *Sci. Adv.* **7**, eabd3632 (2021)
DOI: 10.1126/sciadv.abd3632

This PDF file includes:

Sublimation temperature from kinetic rate laws

Sublimation is an irreversible process governed by kinetics, in contrast to the equilibrium process assumed in conventional condensation models. *Chyba* (*31*) proposed a kinetic rate law to describe the temperature (T) at which kerogen survives heating for a duration (t).

$T = E_a/R[\ln(tA)^{-1}$,

where R is the gas constant, E_a is the activation energy of sublimation, and A is a constant. This Arrhenius equation describes the anti-correlation between temperature and the lifetime of a carbon carrier (Fig. S1). Current theory suggests that during the early stages of proto-stellar evolution accretion events will likely occur in bursts of luminosity with an observationally constrained burst lifetime of order 100 years (*9*). This lifetime is therefore the characteristic heating timescale for the young inner regions of the disk. We calculated that the temperature to sublimate aliphatic hydrocarbon and kerogens as analogues for insoluble organic matter (IOM) in 100 years is 394 K and 478-508 K respectively, using experimentally constrained parameters (*31-32,* Table S1).

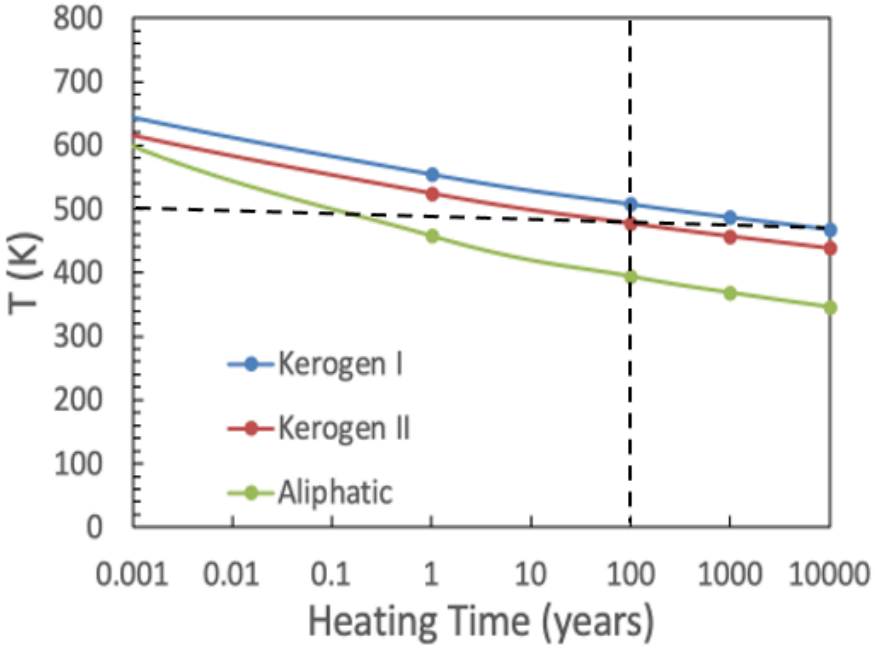

Fig. S1. Kinetic rate law of carbon sublimation. The solid blue, red, and green curves show the sublimation temperature as a function of the heating time during which type I kerogen and type II kerogen (*31*), and aliphatic organics (*32*), respectively, transform into gases. The dashed lines mark the 500 K sublimation temperature for a characteristic heating time of 100 years.

Table S1 Kinetic rate law parameters and calculated sublimation Temperature

	Kerogen Type I (*31*)	Kerogen Type II (*31*)	Aliphatic organics (*32*)
E_a (kJ/mol)	2.31E+05	2.04E+05	1.09E+05
A (s^{-1})	1.70E+14	6.70E+12	8.70E+04
T (K)*	508	478	394

*Sublimation temperature to shed carbon in 100 years

To further examine thermal destruction of IOM in chondrites we plotted the compositional information from Alexander (*33*) as a function of the inferred temperatures from Cody et al. (*34*) in Fig. S2. This exercise is problematic for several reasons, including (a) the data are rather scattered, (b) the normalized decay is very strongly dependent on the assumed initial carbon concentration, (c) the carbon loss is probably a result of thermal or aqueous processing on chondrites, and does not tell us what happens in the dust or in pebbles, and (d) it is not a good assumption that all of these bodies accreted from material with the same initial carbon concentration. Nevertheless, the Alexander-Cody plot shows that upon heating to 300-500 K, chondrites lose 60-70% of its IOM (Fig. S2). This result supports the effective sublimation temperatures of IOM calculated from kinetic rate laws (Table S1).

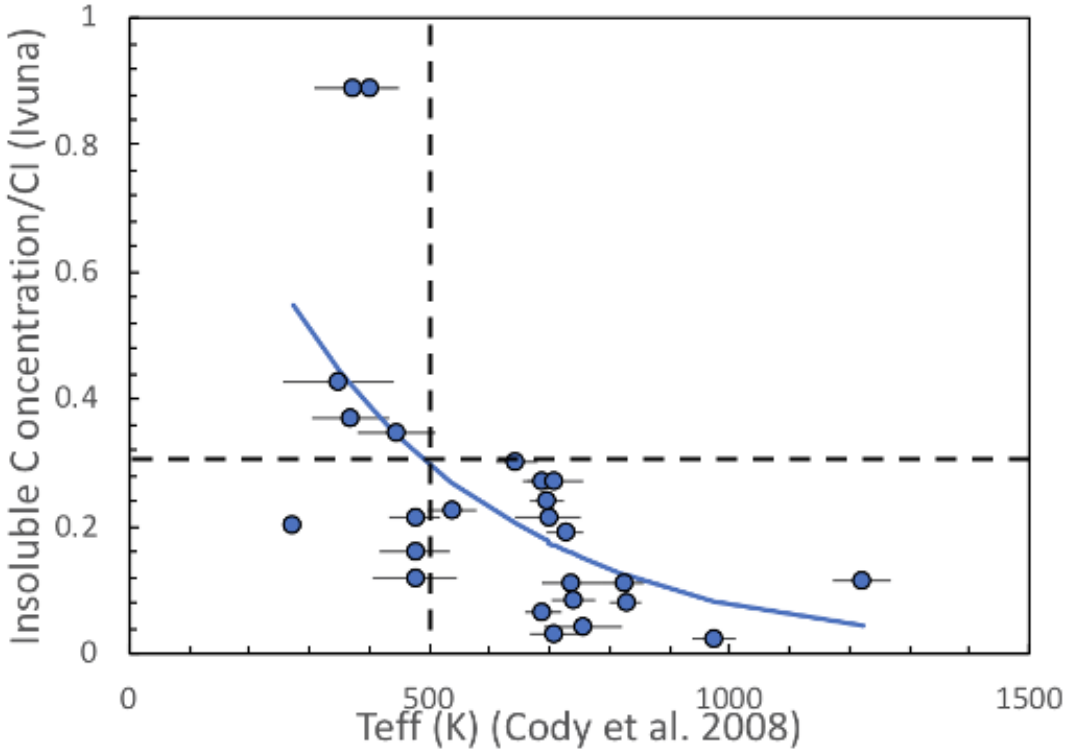

Fig. S2 Amount of insoluble carbon in chondrites as a function of temperature. Insoluble carbon in chondrites, normalized to CI Ivuna with 2.25 wt.% insoluble carbon (*33*) versus Teff, the "Organic Temperature" inferred from the abundance of graphite-like carbon (*34*). Two chondrites, Orgueil (CI) and Tagish Lake (T2) have 2 wt.% C, whilst the others all have no more than half that. The solid blue curve is a fit to a simple exponential function. The dashed lines mark 70% loss of IOM at temperatures below 500 K.

The calculated sublimation temperatures are in general agreement with literature values based on heating experiments (e.g., *4, 35,* Table S2). A number of pyrolysis studies found that some IOM may survive heating in the laboratory at temperature above 500 K in time scales ranging from near-instantaneous to several hours (e.g., *36-38*). However, these studies were not designed to investigate the kinetics of thermal decomposition. Refractory organics may survive for hours or days in a lab, but not weeks to centuries in a nebular disk.

Considering that the refractory organics sublimate in 100 years at 478-508 K (Table S2), we adopt 500 K as the effective sublimation temperature of refractory carbon carriers in the solar nebula. This kinetics-based sublimation temperatures capture the irreversible nature of the transformation of refractory carbon carriers into gases and is used to define the soot line in the disk (Fig. 1 and Fig. S3).

Table S2 Sublimation temperatures of carbon carriers in the solar nebula

Carrier	Sublimation *T*, K	Fraction of solar carbon (Table S5)
CO	35 (*3*)	0.21
CH_4	40 (*3*)	0.0
Other solids	50 (assumed)	0.05
CO_2	80 (*3*)	0.26
CH_3OH	120 (*3*)	0.027
Aliphatic organics	394 (Table S1)	0.05
Aromatic organics	425 (*4*)	0.05
Refractory organics	478-508 (Table S1)	0.30
Amorphous C	1100 (*4*)	0.05
SiC	>1100 (*51*)	2.50E-06
Total		0.997

Disk Modeling

To determine the location of the soot line as a function of time, we calculate the thermal structure within a protoplanetary disk that is heated by internal viscous dissipation and irradiation from the central star. The viscous dissipation is calculated assuming a mass accretion rate as determined by the analytic formula derived by Manara et al. (*39*). The median values are plotted within an envelope representing 0.5 dex ranges given the scatter in the observations (Fig. S3). As the mechanisms for driving the transport of mass in protoplanetary disks remains uncertain, we follow the classical alpha-disk model of Shakura and Sunyaev (*40*) to describe this transport arising from internal viscosity within the gas, adopting alpha=10^{-3}, a value consistent with astronomical constraints (*22, 41*). The thermal profile is calculated assuming an opacity of 1 cm^2/g at all times. The lower bound on the soot line location is represented by the irradiated profile (Fig. S3), where viscous evolution is negligible. For systems with accretion rates below ~10^{-7} $M_\odot$/yr, the midplane temperature due to irradiation only is estimated following the method described in (*22*), using the following expression:

$$T_d(r) = \frac{\frac{1}{2}\phi L_*}{4\pi r^2 \sigma_{SB}}$$

where $T_d(r)$ is the midplane dust or solid temperature as a function of radius r, ϕ is the flaring angle, L_* is the stellar luminosity, and σ_{SB} is the Stefan-Boltzmann constant. Current models of disk observations assume ϕ=0.02 (*22*). For a young solar-mass star on the pre-main sequence, its luminosity at the relevant age of a few Myr is ~2 $L_\odot$ (*42*).

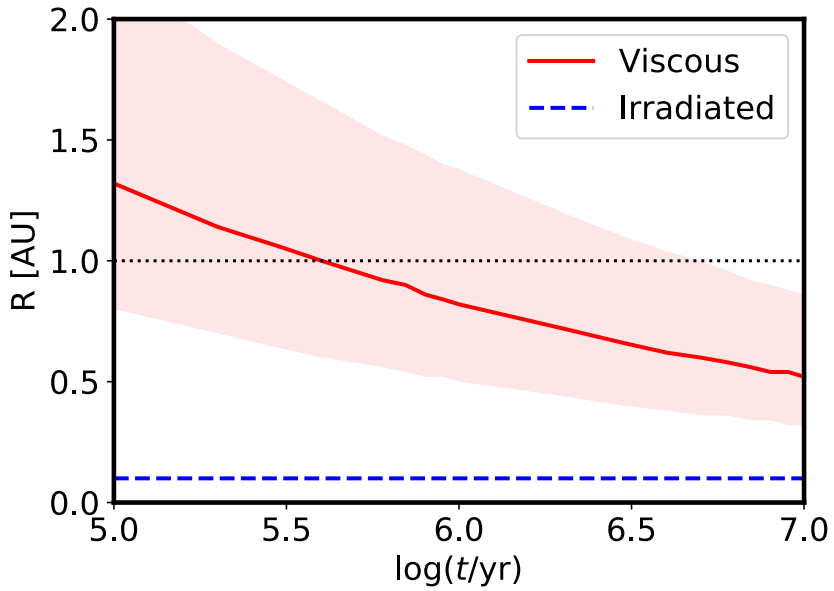

Fig. S3. Migration of the soot line at 500 K with time in a representative protoplanetary disk. The red solid curve traces the location of the soot line moving toward the central star with time in an accretion-dominated disk with a median value of alpha at 10^{-3} within an envelope representing 0.5 dex ranges. The blue dashed line marks the location of the soot line at 0.1 AU in an irradiated disk of a solar-mass star. The black dotted line denotes 1 AU.

We stress that these calculations are conservative in the sense that the calculated disk temperatures are likely too hot. The parameter alpha corresponds to the stress to pressure ratio and controls the rate of internal dissipation. In general, as the gaseous disk dissipates and grains evolve, α will change and the disk cools more efficiently. This is not accounted for in our calculations. The opacity parameter sets how readily heat can diffuse through the disk and get lost to the surroundings. Small grains are the primary source of opacity in disks. As they grow into pebbles and planetesimals over time, the opacity will decrease, making the disks cooler than calculated here. Thus the location of the soot line in the viscous model should be taken as an upper limit, particularly at later times. At t >1 Myr, our simple approach likely overestimates the expected temperatures for an evolving disk and the radiation dominated limit is likely approached.

Bulk silicate Earth composition

The compositions of the bulk silicate Earth (BSE) and CI show striking similarities and obvious differences. Comparison with CI reveals that the relative abundances of refractory elements in the BSE are chondritic but volatile elements are depleted with respective to CI, implying that of the Earth accreted more volatile-poor source materials and/or loss more volatiles through additional processes. To first order, the condensation sequence works for elements that are more volatile than C, but fails to account of the forms and abundances of C in meteoritic and cometary records.

In Fig. 1, an element's relative abundance to Mg and CI is calculated as the ratio of the relative abundance of an element to Mg in BSE to its relative abundance to Mg in CI, so that the relative abundance of Mg, a major element in both the BSE and CI that divides refractory elements and volatile elements, is anchored at 1 (Table S3).

Table S3 Element abundances in bulk silicate Earth

	BSE (*2*) wt.%	BSE relative to Mg	CI (*2*) wt.%	CI relative to Mg	BSE relative to Mg and CI*
O	44	1.93	48.2	4.99	0.39
Mg	22.8	1.00	9.65	1.00	1.00
Si	21	0.92	10.65	1.10	0.83
Fe	6.26	0.27	18.1	1.88	0.15
Ca	2.53	0.11	0.92	0.10	1.16
Al	2.35	0.10	0.86	0.09	1.16
Ni	0.196	0.01	1.05	0.11	0.08
S	0.025	1.10E-03	5.4	0.56	2.0E-03
C	0.014	6.14E-04	3.5	0.36	1.7E-03
Total	99.175		98.33		

*Calculated as the ratio of an element's relative abundance to Mg in BSE to that in CI.

Carbon carriers in the solar nebula

Solid carbon carriers in the solar nebula include ices and refractory phases. The abundance of total carbon in nebular solid is calculated from the solar system composition excluding H and He (Table S4). For comparison with the bulk silicate Earth and Earth, the relative abundance to Mg and CI is used in Fig. 1.

Table S4 Element abundances in the solar system

	Solar (*1*) log A(El)	Solar solid* wt.%	Solar solid relative to Mg	CI (*2*) wt.%	CI relative to Mg	Solar solid relative to Mg and CI#
H	12					
He	10.98					
C	8.46	16.8	3.44	3.5	0.36	9.48
N	7.9	5.4	1.10			
O	8.76	44.8	9.15			
Ne	7.95	8.7	1.77			
Mg	7.62	4.9	0.99	9.65	1.00	0.99
Al	6.54	0.5	0.09	0.86	0.09	1.04
Si	7.61	5.6	1.13	10.65	1.10	1.03
S	7.26	2.8	0.58	5.4	0.56	1.03
Ca	6.41	0.5	0.10	0.925	0.10	1.07
Fe	7.54	9.5	1.93	18.1	1.88	1.03
Ni	6.29	0.6	0.11	1.05	0.11	1.05

*Solar system composition excluding H and He

#Calculated as the ratio of an element's relative abundance to Mg in a solar solid to that in CI.

In Table S5 we provide a list of solid-state carbon carriers (*4, 43*), assuming that 50% of the solar carbon takes refractory forms and 50% would be in the ices at temperatures below 125 K (3). In the sublimation sequence, upon heating CO will be the first to be lost to the gas, whereas in the condensation sequence, upon cooling CO will be the last to transform from gas to solid (Fig. S4). Refractory organics are likely pre-solar (*5*), although some could be created through reactions in the solar nebula (*44-45*). They are not products of condensation from the solar nebula (*1, 3-4*).

Table S5 Carbon carriers in solar nebula

	Fraction of C in ices	Fraction of solar C*	Relative Abundance to Mg (Table S4)	Relative abundance to Mg and CI (Table S4)
Öberg et al. 2011 (*43*)				
CO_2	0.521	0.26	0.895	2.47
CO	0.425	0.212	0.730	2.01
CH_4	0.0	0.0	0.000	0.00
CH_3OH	0.055	0.027	0.094	0.26
	Fraction of C in refractory solids			
Gail and Treiloff 2017 (*4*)				
Refractory organics	0.6	0.3	1.032	2.85
Aromatic organics	0.1	0.05	0.172	0.47
Aliphatic organics	0.1	0.05	0.172	0.47
Amorphous C	0.1	0.05	0.172	0.47
Others	0.1	0.05	0.172	0.47
Alexander et al. 2017 (*51*)				
SiC	5.00E-06	2.50E-06	8.60E-06	2.37E-05

*Assuming 50% in ices, 50% in refractory solids (*3*).

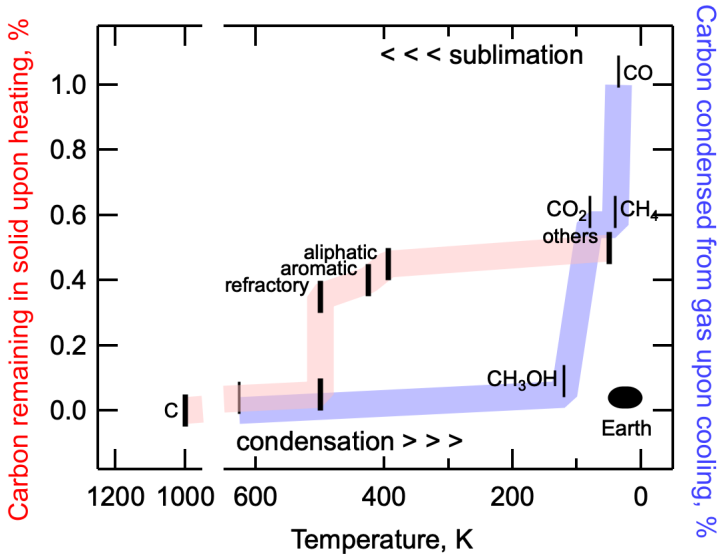

Fig. S4 Sublimation and condensation sequences of carbon in the solar nebula. Upon heating (red trace) the fraction of carbon remaining in dust decreases as ices sublimate at temperatures below 120 K and most refractory carbon carriers (thick vertical bars) in the inherited ISM grains sublimate near a characteristic temperature of ~500 K in 100 years. Upon cooling (blue trace) the remaining fraction of carbon in gas increases but >90% of the gaseous carbon carriers (thin vertical bars) do not condense until the temperature falls below 100 K. The oval in the lower right corner represents the estimated upper bound for the bulk Earth carbon at 0.2-1.9 wt.%, corresponding to 1-7% of the total carbon available in the solar nebula. Data are from Table S2, Table S4, and Table S6.

In a more recent model (*46*), the ISM diffuse cloud dust contains 83 ppm hydrocarbons and 40 ppm PHAs, corresponding to a smaller fraction of aliphatic organics than adopted here (*4*, *47*). Because aliphatics are more volatile and sublimate at relatively low temperature, the differences do not affect our

conclusion. Gail and Treiloff (*4*) isolate a fraction of carbon as highly refractory pure carbon phases (amorphous carbon, graphite, and/or nano-diamonds) with sublimation temperatures greater than 1000 K. This fraction is inferred from an analysis of Comet Halley dust (*48*) and not meteoritic material that survived in the inner solar system such as CI chondrites. In Fig. 1, we do not include this fraction in our sublimation sequence for the inner solar system because the carriers of this signature are amongst the lightest and smallest particles (*4, 48*). At sizes of <0.05 μm, these small particles are readily destroyed in the inner solar system via oxidation near the surface of the disk (*49-50*). Instead, we assume that the highly refractor fraction of C is of order 0.1 x CI with a tail to lower values as temperature increases (Fig. S2). At a baseline level the minimum available amount of highly refractory carbon in the inner solar system is carried by SiC at 5 ppm as traced by meteoritic material (*51*). We note that possible survival of highly refractory carbon at 1100 K would strengthen our conclusion that the Earth's source material lost carbon early in the solar history, when the temperature near 1 au was sufficiently high to remove this component.

Additional constraints on the maximum carbon content of Earth's core

From sound velocities and phase relation: Existing data suggest that the presence of 1.0±0.6 wt.% carbon in liquid iron increases the compressional wave velocity (V_P) of liquid iron to match the observed value of the outer core (Fig. S5), whereas Fe_7C_3 containing as much as 8.4 wt.% carbon can reproduce the anomalously low shear wave velocity (V_S) and liquid-like high Poisson's ratio of the inner core (*52-53*). With 1.0±0.6 wt.% carbon in the outer core and 8.4 w% carbon in the inner core, we obtain an upper bound of 1.3±0.6 wt.% carbon in the core.

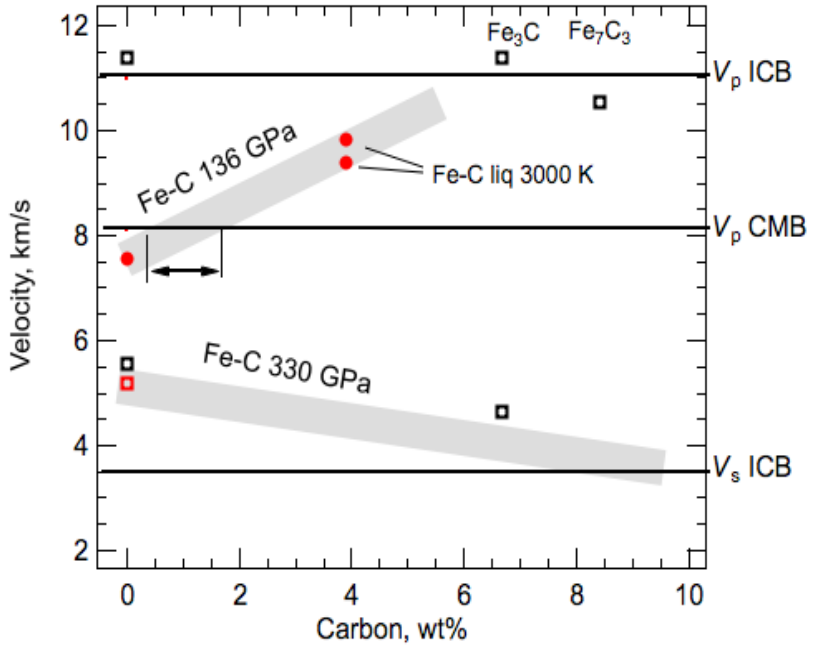

Fig. S5 Upper bound on the carbon content of Earth's core from velocity constraints. The maximum amount of carbon in the liquid outer core is estimated at 1.0±0.6 wt.% (horizontal arrow), assuming that carbon is the only light element responsible for the difference between the sound velocities of iron and that of the core, marked by the horizontal black lines (*16*). The V_P of Fe-C alloy at the inner core boundary (ICB), V_P of Fe-C alloy at the core-mantle boundary (CMB), and V_S of Fe-C alloy at the ICB as a function of carbon content are estimated from that of iron and Fe-C alloys at 330 GPa and 300 K (open black squares along the gray line, *16*), that at 136 GPa and 4500±1500 K (red filled circles along the upper thick gray line, *14-15*) and that at 330 GPa and 5500±1500 K (red open squares along the lower thick gray line), respectively.

With 1.0±0.6 wt.% carbon, outer core composition would fall on the iron-rich side of the eutectic point in the Fe-C binary system (*53-55*, Fig. S6). As a result, an iron-carbon alloy, instead of Fe_7C_3, would be the solid phase to form the inner core. This scenario is supported by studies that found iron carbide too light or too fast for the inner core, and estimated that the inner core contains 1.5 wt.% carbon (*56-59*). In this case, the inner core composition would contain less carbon than the outer core, and therefore the carbon content of the inner core is limited to 1.0±0.6 wt.%. Accordingly, the upper bound for the carbon content of the core is reduced to 1.0±0.6 wt%.

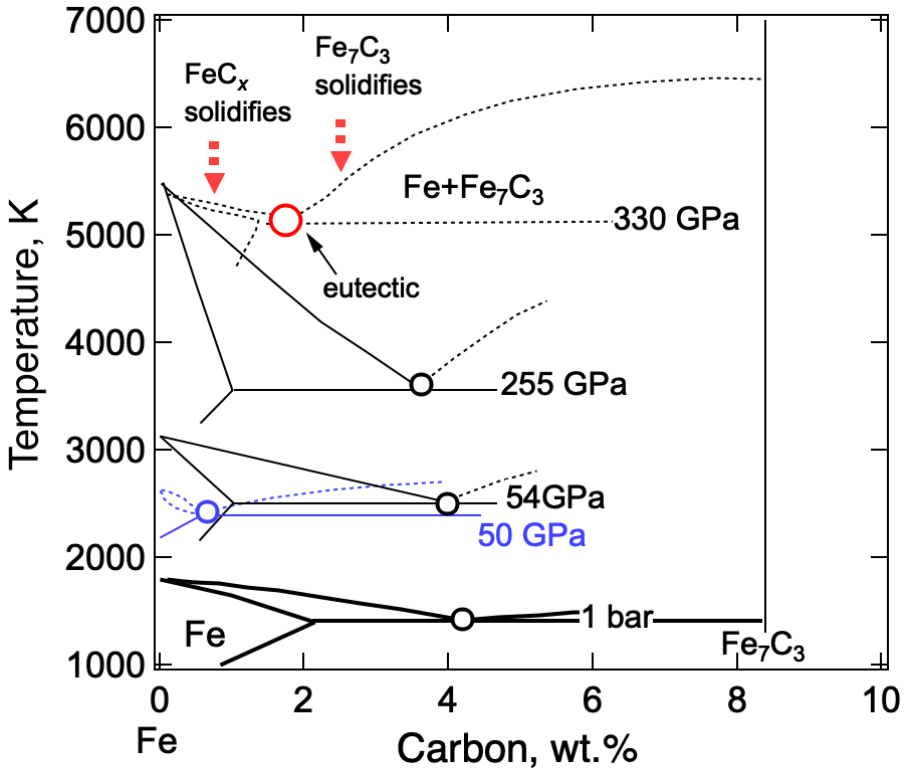

Fig. S6 Constraints on the maximum carbon content of Earth's core from iron-carbon binary phase relation. Existing results at 54-255 GPa (*53*) and 330 GPa (*54*)), with the exception of one result at 50 GPa (Blue, *55*), suggest that the eutectic composition of the Fe-C binary system contain more than 2 wt.% carbon, and therefore an Fe-C alloy, instead of Fe_7C_3, would solidify and form the inner core.

From metal-silicate partitioning: Once accreted to the Earth, the distribution of carbon depends on its partitioning between the iron-rich core and the bulk silicate Earth including the fluid envelope (atmosphere and hydrosphere). The strong affinity of carbon for iron-rich alloys at relatively low pressures suggest that sequestration in the core could be partially responsible for the depletion of carbon in the silicate Earth relative to primitive chondrites (*e.g., 60*), although recent experiments suggest that carbon may become much less siderophile or even lithophile at pressures and temperatures that are relevant to core formation in a deep magma ocean (*12 Fischer*). Using updated parametrization for the partition coefficient of carbon between metal and silicate, Fischer et al. (*12*) obtained an upper bound of 0.1-0.2 wt% in the core, and 370-740 ppm carbon in the bulk Earth. This bulk Earth carbon content overlaps with previous estimates 530±210 ppm for the bulk Earth, derived from an estimate of 765±300 ppm in the bulk silicate Earth and assuming a carbon-free core (*19*). Both values may be viewed as conservative upper bounds and require even larger fractions of carbon-poor building blocks for the Earth.

Table S6 Upper bounds on the carbon content of bulk Earth

	Bulk Silicate Earth (*2*)	Bulk Earth upper bound generous	Bulk Earth upper bound probable	CI (*2*)	C-rich Source material*
C	140±40 ppmw	1.7±0.2 wt.%	0.4±0.2 wt.%	3.5 wt.%	
average	140	1.7	0.4		
+	180	1.5	0.2		
-	100	1.9	0.6		
Relative abundance to Mg: C/Mg					
average	6.14E-04	0.11	0.03	0.36	1.73
+	7.89E-04	0.10	0.01		
-	4.39E-04	0.12	0.04		
Relative abundance to Mg and CI: (C/Mg) / (C/Mg in CI)					
average	1.71E-03	0.30	0.07		4.74
+	2.19E-03	0.27	0.04		
-	1.22E-03	0.34	0.11		
Fraction of C-rich source material in bulk Earth					
average		0.06	0.01		
+		0.06	0.01		
-		0.07	0.02		
Mg, wt.%	22.8	15.4		9.65	

*After C-carrying ices sublimate, the C/Mg ratio is reduced to half of the initial value (Table S2).

Glossary

Aliphatic hydrocarbon: Hydrocarbons based on chains of C atoms, includes alkanes such as methane CH_4, alkenes such as ethene C_2H_4, and alkynes such as acetylene C_2H_2.

Aromatic hydrocarbon: Hydrocarbons containing one or more six-carbon ring as in benzene C_6H_6.

CHON: A mnemonic acronym for the four most common elements in living organisms: carbon, hydrogen, oxygen, and nitrogen. Note that CHON particles refer to kerogen.

Hydrocarbon: Organic chemical compound composed exclusively of hydrogen and carbon atoms such as methane CH_4.

IDP: Interplanetary dust particle, also called micrometeoroid, micrometeorite, or cosmic dust particle, a small grain, generally less than a few hundred micrometers in size and composed of silicate minerals and glassy nodules but sometimes including sulfides, metals, other minerals, and carbonaceous material, in orbit around the Sun.

IOM: Insoluble organic matter. It is major constituent of organic matter in extraterrestrial materials. Includes both the more refractory macromolecular carbon (=CHON=kerogen) as well as the less refractory aromatic and aliphatic hydrocarbons.

ISM: Interstellar medium. the matter and radiation that exists in the space between the star systems in a galaxy. This matter includes gas in ionic, atomic, and molecular form, as well as dust and cosmic rays. It fills interstellar space and blends smoothly into the surrounding intergalactic space.

Kerogen: A solvent-insoluble organic matter in terrestrial rocks. Mainly consists of paraffin hydrocarbon, also called alkane. Has the general formula C_nH_{2n+2}. A terrestrial analog to IOM in meteorites.

Lithophile element: Lithophile means rock-loving. A lithophile element readily combines with oxygen and therefore prefers silicate-rich mantle to iron-rich core. Examples include Mg, Si, Ca, Al, and K.

Macromolecular organics: Including PAHs and insoluble organics matter.

PAH: Polycyclic aromatic hydrocarbon, such as naphthalene $C_{10}H_8$.

Pyrolysis: Thermal Decomposition of materials at high temperatures in an inert atmosphere.

ppm: Parts per million. The number of units of mass of element per million units of total mass

Refractory organics: Predominantly hydrocarbon in nature, with the carbon distributed between the aromatic and aliphatic forms.

Siderophile element: Siderophile means iron-loving. A siderophile element readily alloys with iron and therefore prefers iron-rich core to silicate-rich mantle. Examples include Ni, Au, Pt, S, and C.

REFERENCES AND NOTES

1. K. Lodders, Solar system abundances and condensation temperatures of the elements. *Astrophys. J.* **591**, 1220–1247 (2003).
2. W. F. McDonough, S.-s. Sun, The composition of the Earth. *Chem. Geol.* **120**, 223–253 (1995).
3. E. A. Bergin, L. I. Cleeves, Chemistry during the gas-rich stage of planet formation, in *Handbook of Exoplanets*, H. J. Deeg, J. A. Belmonte, Eds. (Springer, Cham., 2018), pp. 2221–2250.
4. H.-P. Gail, M. Trieloff, Spatial distribution of carbon dust in the early solar nebula and the carbon content of planetesimals. *Astron. Astrophys.* **606**, A16 (2017).
5. C. M. O'D. Alexander, L. R. Nittler, J. Davidson, F. J. Ciesla, Measuring the level of interstellar inheritance in the solar protoplanetary disk. *Meteorit. Planet. Sci.* **52**, 1797–1821 (2017).
6. E. A. Bergin, G. A. Blake, F. Ciesla, M. M. Hirschmann, J. Li, Tracing the ingredients for a habitable earth from interstellar space through planet formation. *Proc. Natl. Acad. Sci. U.S.A.* **112**, 8965–8970 (2015).
7. J. Geiss, Composition measurements and the history of cometary matter. *Astron. Astrophys.* **187**, 859–866 (1987).
8. M. E. Kress, A. G. G. M. Tielens, M. Frenklach, The 'soot line': Destruction of presolar polycyclic aromatic hydrocarbons in the terrestrial planet-forming region of disks. *Adv. Space Res.* **46**, 44–49 (2010)
9. L. Hartmann, G. Herczeg, N. Calvet, Accretion onto pre-main-sequence stars. *Annu. Rev. Astron. Astrophys.* **54**, 135–180 (2016).
10. B. J. Wood, J. Li, A. Shahar, *Carbon in Earth*, R. M. Hazen, A. P. Jones, J. A. Baross, Eds. (Reviews in Mineralogy & Geochemistry, 2013), vol. 75, pp. 231–250 .
11. J. Li, B. Chen, M. Mookherjee, G. Morard, Carbon versus other light elements in Earth's core—A combined geochemical and geophysical perspective, in *Deep Carbon Past to Present*, B. Orcutt, I. Daniel, R. Dasgupta, Eds. (Cambridge Univ. Press, 2019), pp. 40–65.
12. R. A. Fischer, E. Cottrell, E. Hauri, K. K. M. Lee, M. L. Voyer, The carbon content of Earth and its core. *Proc. Natl. Acad. Sci. U.S.A.* **117**, 8743–8749 (2020).
13. G. Morard, Y. Nakajima, D. Andrault, D. Antonangeli, A. L. Auzende, E. Boulard, S. Cervera, A. N. Clark, O. T. Lord, J. Siebert, V. Svitlyk, G. Garbarino, M. Mezouar, Structure and density of Fe-C liquid alloys under high pressure. *J. Geophys. Res. Solid Earth* **122**, 7813–7823 (2017).

14. G. Morard, D. Andrault, D. Antonangeli, J. Bouchet, Properties of iron alloys under the Earth's core conditions. *C. R. Geosci.* **346**, 130–139 (2014).
15. Y. Nakajima, S. Imada, K. Hirose, T. Komabayashi, H. Ozawa, S. Tateno, S. Tsutsui, Y. Kuwayama, A. Q. R. Baron, Carbon-depleted outer core revealed by sound velocity measurements of liquid iron–carbon alloy. *Nat. Commun.* **6**, 8942 (2015).
16. A. M. Dziewonski, D. L. Anderson, Preliminary reference Earth model. *Phys. Earth Planet. In.* **25**, 297–356 (1981).
17. K. Hirose, S. Tagawa, Y. Kuwayama, R. Sinmyo, G. Morard, Y. Ohishi, H. Genda, Hydrogen limits carbon in liquid iron. *Geophys. Res. Lett.* **46**, 5190–5197 (2019).
18. M. M. Hirschmann, Comparative deep Earth volatile cycles: The case for C recycling from exosphere/mantle fractionation of major (H_2O, C, N) volatiles and from H_2O/Ce, CO_2/Ba, and CO_2/Nb exosphere ratios. *Earth Planet. Sci. Lett.* **502**, 262–273 (2018)
19. B. Marty The origins and concentrations of water, carbon, nitrogen and noble gases on Earth. *Earth Planet. Sci. Lett.* **313–314**, 56–66 (2012).
20. S. J. Weidenschilling, J. N. Cuzzi, Formation of planetesimals in the solar nebula, in *Protostars and Planets III* (Univ. Arizona Press, 1993), p. 1031.
21. S. Ida, T. Yamamura, S. Okuzumi, Water delivery by pebble accretion to rocky planets in habitable zones in evolving disks. *Astron. Astrophys.* **624**, A28 (2019).
22. C. P. Dullemond, T. Birnstiel, J. Huang, N. T. Kurtovic, S. M. Andrews, V. V. Guzmán, L. M. Pérez, A. Isella, Z. Zhu, M. Benisty, D. J. Wilner, X.-N. Bai, J. M. Carpenter, S. Zhang, L. Ricci, The Disk Substructures at High Angular Resolution Project (DSHARP). VI. Dust trapping in thin-ringed protoplanetary disks. *Astrophys. J. Letters* **869**, L46 (2018).
23. R. Teague, J. Bae, T. Birnstiel, E. A. Bergin, Evidence for a vertical dependence on the pressure structure in AS 209. *Astrophys. J.* **868**, 113 (2018).
24. P. Pinilla, M. Benisty, T. Birnstiel, Ring shaped dust accumulation in transition disks. *Astron. Astrophys.* **545**, A81 (2012).
25. T. S. Kruijer, C. Burkhardt, G. Budde, T. Kleine, Age of Jupiter inferred from the distinct genetics and formation times of meteorites. *Proc. Natl. Acad. Sci. U.S.A.* **114**, 6712–6716 (2017).
26. S. M. Andrews, J. Huang, L. M. Pérez, A. Isella, C. P. Dullemond, N. T. Kurtovic, V. V. Guzmán, J. M. Carpenter, D. J. Wilner, S. Zhang, Z. Zhu, T. Birnstiel, X.-N. Bai, M. Benisty, A. Meredith

Hughes, K. I. Öberg, L. Ricci, The Disk Substructures at High Angular Resolution Project (DSHARP). I. Motivation, sample, calibration, and overview. *Astrophys. J. Letters* **869**, 2 (2018).

27. M. Flock, J. P. Ruge, N. Dzyurkevich, Th. Henning, H. Klahr, S. Wolf, Gaps, rings, and non-axisymmetric structures in protoplanetary disks from simulations to ALMA observations. *Astron. Astrophys.* **574**, A68 (2015).
28. T. Lichtenberg, G. J. Golabek, R. Burn, M. R. Meyer, Y. Alibert, T. V. Gerya, C. Mordasini, A water budget dichotomy of rocky protoplanets from ^{26}Al-heating. *Nat. Astron.* **3**, 307–313 (2019).
29. J. I. Goldstein, G. R. Huss, E. R. D. Scott, Ion microprobe analyses of carbon in Fe–Ni metal in iron meteorites and mesosiderites. *Geochim. Cosmochim. Acta* **200**, 367–407 (2017).
30. T. Klein, M. Schachermayer, F. Mendez-Martin, T. Schöberl, B. Rashkova, H. Clemens, S. Mayer, Carbon distribution in multi-phase γ-TiAl based alloys and its influence on mechanical properties and phase formation. *Acta Mater.* **94**, 205–213 (2015).
31. C. F. Chyba, P. J. Thomas, L. Brookshaw, C. Sagan, Cometary delivery of organic molecules to the early Earth. *Science* **249**, 366–373 (1990).
32. Y. Kebukawa, S. Nakashima, M. E. Zolensky, Kinetics of organic matter degradation in the Murchison meteorite for the evaluation of parent-body temperature history. *Meteorit. Planet. Sci.* **45**, 99–113 (2010).
33. C. M. O'D. Alexander, M. Fogel, H. Yabuta, G. D. Cody, The origin and evolution of chondrites recorded in the elemental and isotopic compositions of their macromolecular organic matter. *Geochim. Cosmochim. Acta* **71**, 4380–4403 (2007).
34. G. D. Cody, C. M. O'D. Alexander, H. Yabuta, A. L. D. Kilcoyne, T. Araki, H. Ade, P. Dera, M. Fogel, B. Militzer, B. O. Mysen, Organic thermometry for chondritic parent bodies. *Earth Planet. Sci. Lett.* **272**, 446–455 (2008).
35. H. Nakano, A. Kouchi, S. Tachibana, A. Tsuchiyama, Evaporation of interstellar organic materials in the solar nebula. *Astrophys. J.* **592**, 1252–1262 (2003).
36. L. Remusat, S. Derenne, F. Robert, H. Knicker, New pyrolytic and spectroscopic data on Orgueil and Murchison insoluble organic matter: A different origin than soluble? *Geochim. Cosmochim. Acta* **69**, 3919–3932 (2005).
37. C. Vollmer, M. Pelka, J. Leitner, A. Janssen, Amorphous silicates as a record of solar nebular and parent body processes—A transmission electron microscope study of fine-grained rims and matrix in three Antarctic CR chondrites. *Meteorit. Planet. Sci.* **55**, 1491–1508 (2020).

38. M. E. I. Riebe, D. I. Foustoukos, C. M. O'D. Alexander, A. Steele, G. D. Cody, B. O. Mysen, L. R. Nittler, The effects of atmospheric entry heating on organic matter in interplanetary dust particles and micrometeorites. *Earth Planet. Sci. Lett.* **540**, 116266 (2020).
39. C. F. Manara, M. Robberto, N. Da Rio, G. Lodato, L. A. Hillenbrand, K. G. Stassun, D. R. Soderblom, *Hubble Space telescope* measures of mass accretion rates in the Orion nebula cluster. *Astrophys. J.* **755**, 154 (2012).
40. N. I. Shakura, R. A. Sunyaev, Black holes in binary systems: Observational appearances, in *X- and Gamma-Ray Astronomy* (1973), p. 155.
41. K. Flaherty, A. M. Hughes, J. B. Simon, C. Qi, X.-N. Bai, A. Bulatek, S. M. Andrews, D. J. Wilner, Á. Kóspál, Measuring turbulent motion in planet-forming disks with ALMA: A Detection around DM tau and nondetections around MWC 480 and V4046 Sgr. *Astrophys. J.* **895**, 109 (2020).
42. I. Baraffe, D. Homeier, F. Allard, G. Chabrier, New evolutionary models for pre-main sequence and main sequence low-mass stars down to the hydrogen-burning limit. *Astron. Astrophys.* **577**, A42 (2015).
43. K. I. Öberg, A. C. A. Boogert, K. M. Pontoppidan, S. van den Broek, E. F. van Dishoeck, S. Bottinelli, G. A. Blake, N. J. Evans II, The *Spitzer* ice legacy: Ice evolution from cores to protostars. *Astrophys. J.* **740**, 109 (2011)
44. M. Kuga, B. Marty, Y. Marrocchi, L. Tissandier, Synthesis of refractory organic matter in the ionized gas phase of the solar nebula. *Proc. Natl. Acad. Sci. U.S.A.* **112**, 7129–7134 (2015).
45. R. Tartese, M. Chaussidon, A. Gurenko, F. Delarue, F. Robert, Insights into the origin of carbonaceous chondrite organics from their triple oxygen isotope composition. *Proc. Natl. Acad. Sci. U.S.A.* **115**, 8535–8540 (2018).
46. B. T. Draine, B. S. Hensley, The dielectric function of "Astrodust" and predictions for polarization in the 3.4μm and 10μm features. arXiv:2009.11314 [astro-ph.GA] (23 September 2020).
47. A. P. Jones, Dust evolution, a global view: IV. Tying up a few loose ends. arXiv:1804.10628 [astro-ph.GA] (27 April 2018).
48. M. N. Fomenkova, On the organic refractory component of cometary dust. *Space Sci. Rev.* **90**, 109–114 (1999).
49. D. E. Anderson, E. A. Bergin, G. A. Blake, F. J. Ciesla, R. Visser, J.-E. Lee, Destruction of refractory carbon in protoplanetary disks. *Astrophys. J.* **845**, 13 (2017).

50. L. Klarmann, C. W. Ormel, C. Dominik, Radial and vertical dust transport inhibit refractory carbon depletion in protoplanetary disks. *Astron. Astrophys.* **618**, 10.1051/0004-6361/201833719 (2018).
51. C. M. O'D.Alexander, G. D. Cody, B. T. De Gregorio, L. R. Nittler, R. M. Stroudc, The nature, origin and modification of insoluble organic matter in chondrites, the major source of Earth's C and N. *Chem. Erde-Geochem.* **77**, 227–256 (2017).
52. C. Prescher, L. Dubrovinsky, E. Bykova, I. Kupenko, K. Glazyrin, A. Kantor, C. Mc Cammon, M. Mookherjee, Y. Nakajima, N. Miyajima, R. Sinmyo, V. Cerantola, N. Dubrovinskaia, V. Prakapenka, R. Rüffer, A. Chumakov, M. Hanfland, High Poisson's ratio of Earth's inner core explained by carbon alloying. *Nat. Geosci.* **8**, 220–223 (2015).
53. I. Mashino, F. Miozzi, K. Hirose, G. Morard, R. Sinmyo, Melting experiments on the Fe-C binary system up to 255 GPa: Constraints on the carbon content in the Earth's core. *Earth Planet. Sci. Lett.* **515**, 135–144 (2019).
54. Y. Fei, E. Brosh, Experimental study and thermodynamic calculations of phase relations in the Fe-C system at high pressure. *Earth Planet. Sci. Lett.* **408**, 155–162 (2014).
55. O. T. Lord, M. J. Walter, R. Dasgupta, D. Walker, S. M. Clark, Melting in the Fe-C system to 70 GPa. *Earth Planet. Sci. Lett.* **284**, 157–167 (2009).
56. L. Vočadlo, J. Brodholt, D. P. Dobson, K. S. Knight, W. G. Marshall, G. D. Price, I. G. Wood The effect of ferromagnetism on the equation of state of Fe 3 C studied by first-principles calculations. *Earth Planet. Sci. Lett.* **203**, 567–575 (2002).
57. S. Ono, K. Mibe, Magnetic transition of iron carbide at high pressures. *Phys. Earth Planet. In.* **180**, 1–6 (2010).
58. M. Mookherjee, Elasticity and anisotropy of Fe_3C at high pressures. *Am. Mineral.* **96**, 1530–1536 (2011).
59. K. D. Litasov, I. S. Sharygin, P. I. Dorogokupets, A. Shatskiy, P. N. Gavryushkin, T. S. Sokolova, E. Ohtani, J. Li, K. Funakoshi, Thermal equation of state and thermodynamic properties of iron carbide Fe_3C to 31 GPa and 1473 K. *J. Geophys. Res. Solid Earth* **118**, 5274–5284 (2013).
60. H. Chi, R. Dasgupta, M. S. Duncan, N. Shimizu, Partitioning of carbon between Fe-rich alloy melt and silicate melt in a magma ocean—Implications for the abundance and origin of volatiles in Earth, Mars, and the Moon. *Geochim. Cosmochim. Acta* **139**, 447–471 (2014).